C. R. Physique 16 (2015) 789–801

Contents lists available at ScienceDirect

Comptes Rendus Physique

www.sciencedirect.com

Radio science for connecting humans to information systems / L'homme connecté

Body area networks at radio frequencies: Creeping waves and antenna analysis

Réseaux de communication corporels aux fréquences radio : ondes rampantes et analyse des antennes

Khaleda Ali [a], Farshad Keshmiri [b], Alessio Brizzi [a], Yang Hao [a], Christophe Craeye [c,*]

[a] *Queen Mary University London, Electrical Eng. Dept., Mile End Road, E1 4NS London, UK*
[b] *ART-FI, 27, rue Jean-Rostand, Parc Club Orsay Université, 91400 Orsay, France*
[c] *Université catholique de Louvain, place du Levant, 3, ICTEAM Institute, Louvain-la-Neuve, Belgium*

ARTICLE INFO

Keywords:
Body area networks
Creeping waves
Antennas

Mots-clés :
Réseaux corporels
Ondes rampantes
Antennes

ABSTRACT

On-body communication technology development requires a better knowledge of antenna radiation and wave propagation along the body, in both near and far fields. Therefore, Green's functions associated with penetrable cylinders are briefly reviewed, considering frequencies at which the body is not much larger than the wavelength and with a particular attention given to the near fields. A unified approach based on current sheets is provided and an acceleration technique is proposed. This is validated with the help of an FDTD software, which also allows the analysis of non-canonical cross-sections. The properties of creeping waves launched by sources parallel and perpendicular to the body are studied, in particular from the point of view of their phase velocity, and a very simple fitting model is proposed. It is also explained how the Green function can be exploited to analyze antennas very efficiently with the help of an integral-equation approach.

RÉSUMÉ

La technologie de communication corporelle nécessite une meilleure connaissance du rayonnement des antennes et de la propagation le long du corps humain, tant en champs proches qu'en champs lointains. Par conséquent, les fonctions de Green associées aux cylindres pénétrables sont brièvement revues pour des fréquences où le corps n'est pas beaucoup plus grand que la longueur d'onde, avec une attention particulière portée aux champs proches. Une approche unifiée, fondée sur des nappes de courant, est adoptée, et une technique d'accélération est proposée. Ceci est validé à l'aide d'un logiciel FDTD, qui permet aussi l'analyse de sections non canoniques. Les propriétés des ondes rampantes excitées par des sources parallèles et perpendiculaires au corps sont étudiées : en particulier, leur vitesse de phase. Un modèle d'interpolation très simple est proposé.

* Corresponding author.
E-mail addresses: khaleda.ali@qmul.ac.uk (K. Ali), farshad.keshmiri@art-fi.eu (F. Keshmiri), a.brizzi@qmul.ac.uk (A. Brizzi), yang.hao@eecs.qmul.ac.uk (Y. Hao), christophe.craeye@uclouvain.be (C. Craeye).

http://dx.doi.org/10.1016/j.crhy.2015.10.005
1631-0705/

Nous expliquons également comment les antennes en présence du corps peuvent être analysées en exploitant les fonctions de Green via la résolution d'équations intégrales.

1. Introduction

Over the past 20 years, the flexibility of wireless communications allowed a technological revolution. This is how smartphones, with ever increasing contents and applications, are now being used by practically everyone in developed countries. This trend is now extending to machine-to-machine communications and to the "internet-of-things", where objects can interact with each other via the web. In this context, the human body becomes more and more intimately connected with the rest of the world. This is even true for different parts of the human body, which may get connected with each other and with their environment. For instance, physiological data from the different parts of the body can be gathered at one point of the same body before being sent outward; the reverse path can also be followed, from an external source to different points along the body surface.

To further develop on-body communications, it is important to know how the waves propagate along the human body [1–3] and how the body behaves as a propagation channel [4,5]. Moreover, it is useful to investigate how such waves can be efficiently transmitted or received when the antennas are placed very close to the body [6–8]. The latter point includes the dramatic change of behavior of antennas when placed very close to the body surface, which can be mitigated using specific designs [9,10]. This calls for an accurate representation of fields radiated by sources located near the human body, in both near and far fields. In order to gain physical insight into the related radiation mechanisms and in order to avoid very time-consuming numerical simulations, the answer to the above question requires a certain level of approximation regarding the representation of the body. In many publications about "body area networks", that approximation consists in representing the human torso, or the whole human body, as a cylinder [11–13], as sketched in Fig. 1; skeletons made of multiple cylinders have also been considered [14,15].

In this paper, we will first briefly review the fast and accurate calculation of the Green function of the Helmholtz wave operator [16,12] in the presence of a penetrable cylinder, i.e. a cylinder with finite permittivity and conductivity and with dimensions representing an adult human body. In other words, what is computed is the field around the body when it is illuminated by a point-like current source located in its vicinity, considering different orientations of the source. Thanks to the introduction of new boundary conditions, a unified approach, in which sources are decomposed into current sheets, will be made possible for all source polarizations. Special attention will be given to the field in the immediate vicinity of the source, which will be important for antenna analysis. The Green function formulation will then be validated with the help of the FDTD (Finite Difference Time Domain) method [17] at relatively low frequencies of a few gigahertz, corresponding to popular communication standards, at which the cylinder radius is not much larger than the wavelength. Finally, we will explain how the Green function can be exploited to efficiently calculate the behavior of antennas placed very close to the human body. This can be done while considering a computational domain strictly limited to the surface of the antennas, while the presence of the body will be implicitly accounted for through the use of the Green function. That will be explained considering dipoles, i.e. canonical antennas. There, from the numerical point of view, the importance of treating separately the incident and scattered fields will be stressed, since it eases the treatment of near-field singularities. From the physical point of view, a useful result of such an analysis is the transmittance between antennas, without having to handle the difficult question of which definition to consider for the radiation pattern of an antenna located very close to the body. An overview of more complex antennas, specifically devoted to BAN applications, will also be provided.

The remainder of this paper is organized as follows. In Section 2, the main ideas underlying the Green function's calculation are reviewed and a way of accelerating the computation is described. Section 3 validates this approach using the FDTD method. The latter will be used considering cylinders with cross-sections that are either circular or elliptical, in order to also provide more insight into the correlation between propagating EM waves and body shape variations. Section 4 explains

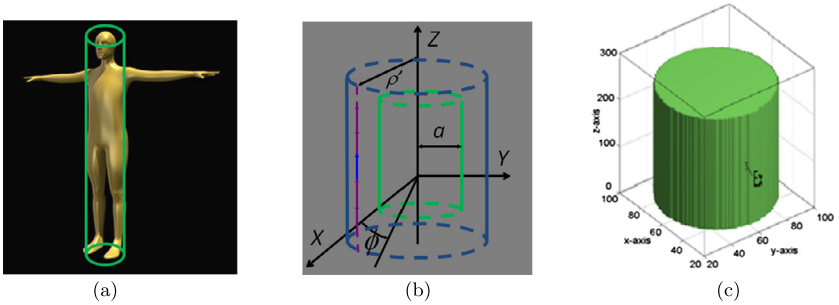

(a) (b) (c)

Fig. 1. (Color online.) (a) Human body and equivalent cylinder, (b) cylinder and cylindrical current sheet, (c) voxelized cylinder used in FDTD simulations.

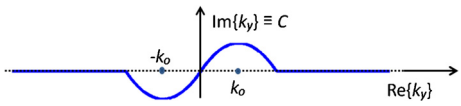

Fig. 2. (Color online.) Sketch of parabolic integration contour in complex k_z plane.

how the Green functions can be exploited to calculate the transmittance between canonical antennas located close to the body. Conclusions are drawn in Section 5.

2. Body Green's function

In this section, we briefly review the Green function analysis in the presence of the human body, modeled as a cylinder with radius a (inner cylinder in Fig. 1b), illuminated by a source at distance ρ' from its axis. The fields are decomposed into TE^z and TM^z cylindrical waves, which respectively have zero components of electric and magnetic fields along z. As explained in [18] and as recalled in Appendix A, all fields components can be derived from the H_z and E_z components for TE^z and TM^z modes, respectively.[1] This is why those components are first derived in the form of cylindrical waves. For instance, for the TM mode, one has:

$$H_z = \frac{1}{2\pi} \int_{-\infty}^{\infty} \sum_m F(m, k_z)\, \mathrm{e}^{\mathrm{j}\, m\, \phi}\, B_m(k_\rho\, \rho)\, \mathrm{e}^{-\mathrm{j}\, k_z\, z}\, \mathrm{d}k_z \tag{1}$$

where the B_m function corresponds to the Hankel function $H_m^{(2)}$, except for fields incident on the cylinder for $\rho < \rho'$, for which B_m corresponds to the Bessel function J_m, while $k_z^2 + k_\rho^2 = k^2$, where k is the free-space wavenumber. A physical interpretation of representation (1) consists in decomposing first the point source into line sources [11] with unit amplitude and a phase progression expressed by wavenumber k_z (vertical line with arrows in Fig. 1b). For a specific wavenumber k_z, such a line source radiates a cylindrical wave away from the axis of the line source. That wave is propagating for $|k_z| < k$ and evanescent for $|k_z| > k$. It is important to notice that a pole appears in the electric field for $k_z = k$. This prevents a straightforward numerical integration. Hence, the analytical extension of k_z to the complex plane needs to be considered. An often-used path corresponds to an elliptic one around the pole [19]. However, the derivative of that contour introduces a spurious singularity at the start and end points of the half ellipse. This is why we chose a parabolic contour [11], sketched in Fig. 2. The contour should be wide enough to avoid any possible pole on the real axis. With such a representation, the incident fields from the line source are still not described in a geometry that conforms the circular contour of the scatterer. Here, a possible approach exploits the addition theorem of Hankel functions: it allows one to decompose cylindrical waves described around one given axis (here the line source) into cylindrical waves around another axis [20,21] (here the axis of the cylinder). This has been exploited in [22] and [12] to study the scattering by a cylindrical body. An alternative approach, used in [11], consists of extending the methodology described above to decompose the point source into line sources. Now, each line source is decomposed into cylindrical sheets. Such a sheet has the same axis as the cylinder and contains the line source (see outer cylinder in Fig. 1b). In view of its great simplicity and its physical grounds, this is the approach summarized here.

The current sheets, characterized by both spectral coordinates k_z and m radiate fields inwards as well as outwards. Those radiated inwards, superimposed to the scattered fields, need to satisfy the boundary conditions at the surface of the cylinder (see below). The fields from the sheet source and the scattered fields are both expressed through a decomposition of the form (1). In the following, the integration and summation will be omitted, while the exponentials will be implicitly assumed.[2] The fields radiated by the current sheets are obtained by imposing the proper boundary conditions across the current sheet. For sources parallel to the cylinder, the boundary conditions simply consist of the well-established continuity of the tangential electric field and the jump conditions of the tangential magnetic field. Algebraically, for cylindrical harmonics, those conditions are enforced via the use of the Wronskian of Bessel functions [18]

$$J'_m(x)\, H_m^{(2)}(x) - J_m(x)\, H_m^{(2)'}(x) = \frac{2\,\mathrm{j}}{\pi\, x} \tag{2}$$

for $x = k_\rho\, \rho'$. This has been done in detail in [11] for source currents that are parallel to the cylinder surface. It is not obvious which boundary conditions need to be satisfied when the current sheet is made of currents that are normal to the surface. In this case, a first option consists in resorting to the – more traditional – use of the addition theorem [23], also exploited in [14]. A potential-based derivation is described in [12] for sources in arbitrary polarizations. In those approaches, the derivations are very long and the final expressions remain complex. To overcome those limitations, boundary conditions applicable to the case of normal currents are proposed below; this in turn allows a very quick derivation of all

[1] In the following, the z superscript will be omitted in TE^z and TM^z.

[2] Hence, deriving w.r.t. z and ϕ amounts to multiplying by $\mathrm{j}m$ and $-\mathrm{j}k_z$, respectively.

field components, following the same procedure as for tangential sources [11]. This will be described below using the same notation as in [11]. To obtain the new boundary conditions for normal currents, fields are integrated over a very small surface crossing the interface, similarly to the procedure employed to prove usual boundary conditions. The integrand here corresponds to the magnetic-field wave equation. The followed procedure is, to a large extent, similar to that often used to obtain the scalar potential associated with a point source ([16], Sec. 3.12). To alleviate the explanations, the details of the proof are provided in Appendix B. The spectral representation (cf. (1)) for the current density is, as in [11], $J = I\,\delta(\rho-\rho')/\rho'$. Then, denoting as ΔP the difference between field P just outside and just inside the current sheet, the resulting boundary conditions read:

$$\text{TM: } \Delta E_z = \mathrm{j}\,\frac{\eta}{k}\,\frac{\partial I}{\partial z}\,\frac{1}{\rho'}; \qquad \text{TE: } \Delta\,\frac{\partial H_z}{\partial \rho} = \frac{\partial I}{\partial \phi}\,\frac{1}{\rho'^2} \tag{3}$$

The following physical interpretations are possible: in the TM case, the non-zero E_z component arises from consecutive dipoles collectively radiating at an angle as a result of their phase shift along $\hat{z}$; in the TE case, the non-zero H_z component arises from uncompensated magnetic fields radiated from dipoles that are phase-shifted along ϕ. With the boundary conditions (3), the z component of the fields can be immediately established. As explained above, the Wronskian of Bessel functions is a very convenient tool. To guide the reader, the procedure will be followed here in detail for the TE case. The incident fields read:

$$H_z = F_m^{\circ}\,H_m^{(2)}(k_\rho\,\rho')\,J_m(k_\rho\,\rho) \;\text{ for }\; \rho<\rho'; \qquad H_z = F_m^{\circ}\,J_m(k_\rho\,\rho')\,H_m^{(2)}(k_\rho\,\rho) \;\text{ for }\; \rho>\rho' \tag{4}$$

From there, the jump condition on $\partial H_z/\partial\rho$ is directly expressed as:

$$-k_\rho\,F_m^{\circ}\left(J_m'(k_\rho\,\rho')\,H_m^{(2)}(k_\rho\,\rho') - J_m(k_\rho\,\rho')\,H_m^{(2)'}(k_\rho\,\rho')\right) = \frac{\mathrm{j}\,m}{\rho'^2}\,I \tag{5}$$

where the parenthesis obviously corresponds to the Wronskian (2) for $x = k_\rho\,\rho'$. From there, one immediately obtains $F_m^{\circ} = -m\,\pi\,I/(2\rho')$, and hence the first equation below:

$$H_z = -\frac{m\,\pi}{2\,\rho'}\,H_m^{(2)}(k_\rho\,\rho')\,J_m(k_\rho\,\rho)\,I; \qquad E_z = \frac{\eta\,k_z\,k_\rho\,\pi}{2\,\mathrm{j}\,k}\,H_m^{(2)'}(k_\rho\,\rho')\,J_m(k_\rho\,\rho)\,I \tag{6}$$

while the second one, applicable to the TM case, results from the application of the first jump condition in (3) through a similar reasoning. Both results have been given for $\rho<\rho'$, since the fields will be needed for $\rho = a < \rho'$, where boundary conditions need to be enforced. The above results are perfectly consistent with those found (after more lengthy derivations) in [24]. Expressions for E_z and H_z for the case of sources tangential to the cylinder are found in [11], where the Wronskian has been exploited in a similar way.

For each harmonic (each value of m and k_z), one needs to determine the scattered TE and TM fields, which are in the from of $F_m\,H_m^{(2)}(k_\rho\,\rho)$ with $F_m = A'$ for denoting the E^z field in the TM case and $F_m = B'$ for denoting the H^z field in the TE case. Similarly, the total fields inside the cylinder are represented using constants $C = A$ and $C = B$, while the Hankel function is replaced by a Bessel function because the domain contains the origin [20]. The vector of coefficients $\mathbf{p} = [A\;A'\;B\;B']^{\mathrm{T}}$ is obtained by imposing the continuity of the tangential electric and magnetic fields across the boundary of the cylinder. For a given (m, k_z) pair, the resulting system of equations reads:

$$\mathbf{M}\,\mathbf{p} = \mathbf{f}^i \tag{7}$$

where vector $\mathbf{f}^i$ describes the tangential incident fields from the current sheet: $\mathbf{f}^i = [E_z^i\;H_\phi^i\;E_\phi^i\;H_z^i]^{\mathrm{T}}$. The components of matrix $\mathbf{M}$ are obtained by expressing, for the given harmonic, the tangential components of the fields from their axial components ([18], Appendix A) described by $\mathbf{p}$. This derivation is a bit tedious and we refer the reader to [11] for finding all the entries of the matrix. This is fundamentally different from the two independent 2×2 systems of equations obtained when studying scattering by planar interfaces [25]. That is due to the fact that TE and TM fields do couple with each other. In other words, in general, TE incident fields will give rise to both TE and TM scattered fields.

Numerous studies [8,26,23,13,14,27,28] indicated, theoretically as well as experimentally, that waves launched by sources perpendicular to the surface exhibit a slower decay along the body surface. This can be traced back to the excitation of TM Zenneck waves [29,30], at intermediate distances and Norton waves [31,1], at larger distances, which have also been observed in the case of flat phantoms at high frequencies in [32]. Ultra-wideband antennas exploiting this phenomenon are described in [33]. Further insight into those creeping waves can be gained by studying the fields for distances large in terms of wavelengths, as it becomes necessary at high frequency. In this case, asymptotic expansions can be used [34,29,35]. This allows the determination of the behavior of the fields far from the transmitting antennas, as detailed in [13,2,3], where an excellent correlation between results obtained with this approach and measurements has been shown for observation points beyond a few wavelengths from the source, around the cylindrical surface.

It is interesting to realize that estimating the Green function over whole volumes or surfaces does not take much more time than at just one point. Indeed, once the coefficients A, A', B and B' have been determined (see equation (7) and paragraph above) for all cylindrical harmonics k_z and m, the fields can be obtained everywhere by propagating all the

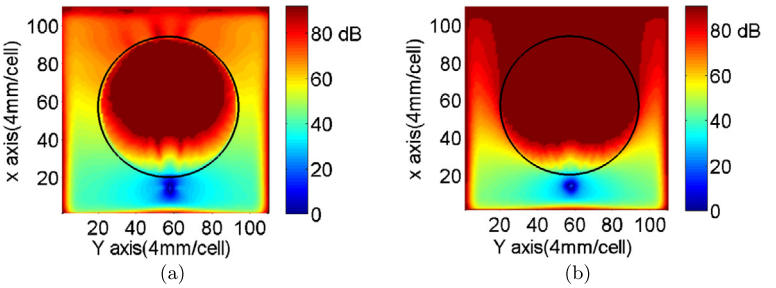

Fig. 3. (Color online.) Path loss for an electric field (a) perpendicular to the body and (b) parallel to the body (dB scale). Radius $a = 15$ cm.

harmonics. For instance, for observation along a given radius ρ but for varying values of z and ϕ, the field computation can be carried out in the following newly proposed matrix form (ϕ along rows and z along columns):

$$\mathbf{V} = \mathbf{FSD} + \mathbf{V}^i \tag{8}$$

where $\mathbf{V}^i$ is the incident field, $F(n_\phi, m) = e^{j\,m\,\phi}$, $S(m, n_k) = A'(k_z, m)\, H_m^{(2)}(k_\rho\, \rho)$, $D(n_k, n_z) = \mathrm{e}^{-\mathrm{j}\,k_z\,z}\,(1 + j\,C')\,\Delta k_z/\pi$, where function C links the imaginary and real parts of k_z (see Fig. 2). An important remark needs to be made regarding incident fields. One should also note that, using the approach described above, if the incident field is observed at the same radius $\rho = \rho'$ as the source, its harmonic decomposition does not converge well. However, to obtain the scattered field, the incident field needs to be decomposed into cylindrical harmonics only at the level of the cylinder surface, i.e. for $\rho = a$, while incident fields elsewhere can be expressed directly in closed form as the fields due to point sources in free space [36]. This enables the fast and accurate simulation assuming a cylindrical model for the body. Other configurations are of interest to BAN communications, such as scattering by multiple cylinders and by elliptical cylinders, studied in [14] and [37], respectively. Finally, one should remark that it would also be interesting to analyze magnetic sources, in order to provide a fundamental insight into the fields radiated by slot antennas, as can be found in the designs proposed in [38,39] and [40].

3. FDTD analysis of creeping waves

The Finite Difference Time Domain [41,17] technique (FDTD) is one of the most suitable numerical methods in the domain of computational electromagnetics, particularly for investigating on-body channel characteristics [7]. Initially, this numerical tool has been used to estimate SAR (Specific Absorption Rate) in mobile communications [42]. Later, extensive study has been performed using FDTD considering different numerical phantoms [43–45] in on-body communication scenarios. This method is used here to validate the Green functions referred to above and to allow the analysis of wave propagation while considering cross-sections other than circular. An in-house parallel FDTD software [46–48] will be used here at the relatively low frequency of 2.4 GHz, at which the wavelength is not much smaller than the body's cross-section. The human torso has been approximated as a uniformly shaped homogeneous lossy cylinder, as shown in Fig. 1c. The dielectric properties of the cylinder are considered to be similar to those of muscle tissue, with conductivity $\sigma = 2.21$ S/m and relative permittivity $\epsilon_r = 47$ [49].

Firstly, the simulation is performed using a circular cylinder of perimeter 94 cm. Later the study has been extended using three other elliptical cylinders representing the torso with different major (2a) to minor axis (2b) ratios. The electric sources are positioned along the major axis (2a) of the torso. The axial ratio (a/b) of the models with the major axis are considered as 1.15, 1.5 and 2. It is worth mentioning that the parameters of the elliptical cylinders are considered to be similar to those of the real dimensions of a human body. The heights of the cylinders are set to 1 m. The transmitting source is a single-cell point source, placed 3 cm away from the trunk (cylinder) along the radius at a height of 0.5 m. To simulate such a cylinder in the FDTD domain, firstly it has been converted into a volumetric mesh with each cell of 4 mm (1/30th of free space wave length, see Fig. 1c) using the Binvox [50] open-source software. The cell size has been kept small in order to minimize the staircase effect caused by analyzing curved subjects in the FDTD domain. To simulate a volume of $110 \times 110 \times 280$ cells, the required computational time was around 30 min. The PC cluster used includes one monitoring node and 15 nodes[3] for accomplishing the simulation. The closer the point source is to the surface, the stronger the radiated field will be on the entire body surface. To analyze the effect of different polarizations in a creeping-wave propagation scenario, two different cases have been taken into account: firstly when the source has been positioned in normal direction to the body (E_x) and secondly when the transmitter is placed parallel to the body (E_z), as can be seen in Figs. 3a and 3b. Both of these figures indicate the path-loss distribution in and around the cross section of the human body (circular cylinder). The unit of the color gradients is the dB. Hence lower values in dB designate lower path losses and higher values in dB represent higher path losses. It is observed that for the source placed perpendicular to the body, the path loss around the curvature

[3] Each node has a Dual Intel Xeon E5405 (Quad Core 2.0 GHz) central processing unit (CPU). There are 128 cores and 512 GB memory in total providing 4 GB at each processor

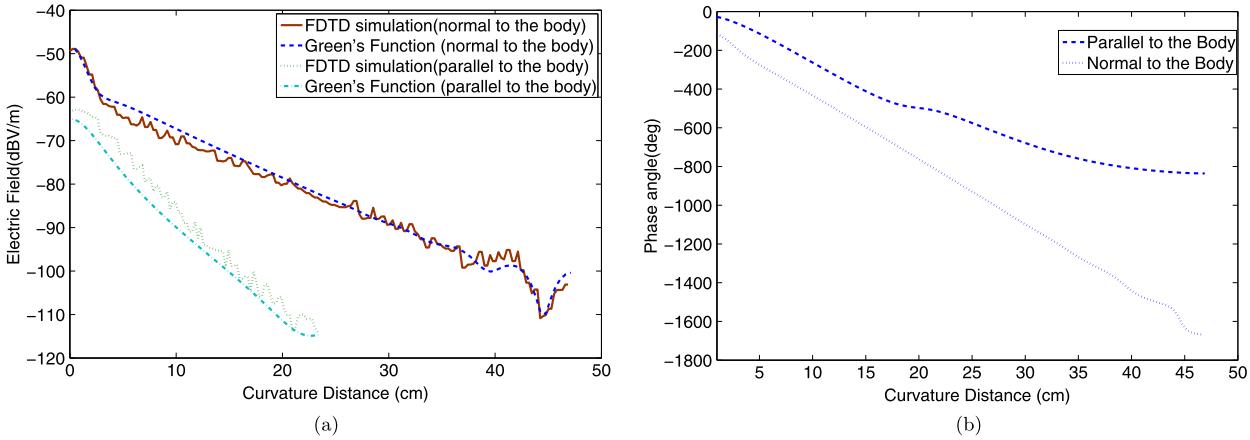

Fig. 4. (Color online.) (a) Comparison between Green's functions and FDTD results, (a) magnitude, (b) phase. Radius $a = 15$ cm.

is relatively low (as in Fig. 3a) compared to the case when the source is parallel to the body (as shown in Fig. 3b [8]). Similarly, it is observed from Fig. 4a that when the source is normal to the body, the magnitude of the electric field falls off at a much lower rate than when the source is parallel to the body. To estimate more precisely the degree of variation of the field distribution along the boundary, the magnitude of the normal and parallel components of the electric fields around the curvature of the body are monitored. Comparison has been made between the results obtained from FDTD and Green's functions approaches for both polarizations of the sources. Fig. 4 indicates a good agreement in both magnitude and phase of the electric field's components. It is observed from the simulated results that for the normally directed source, initially the signal strength falls off at a rapid rate within a few centimeters. Later, the signal starts to decrease at a lower decay rate. This can be defined as the creeping wave region where the lossy cylinder guides the fields to a certain extent. This is evident when at 20 cm distance, for perpendicular polarization, the electric field is near -80 dBV/m, whereas for parallel polarization it falls down to almost -120 dBV/m (as in Fig. 4a).

The creeping wave in an on-body communication scenario can also be identified in terms of its phase constant and phase velocity [51]. The phase constant β (in rad/cm) can be evaluated from the slope of the plotted curve in the creeping wave region (see Fig. 4b). The phase velocity can be estimated from the phase constant as $v_{\mathrm{ph}} = \omega/\beta$, with ω the radian frequency. It can be estimated from Fig. 4b, for instance, where phases for the vertical case are not truly reliable for distances where the magnitude becomes very low (dotted). The associated phase velocity estimate is 0.89 and 0.98 times the speed of light, respectively, for normal and parallel directions of the source with respect to the body. This clearly indicates that, for a normally directed source, at least in this frequency domain, the phase velocity of the creeping wave is substantially lower than the speed of light, which is typical of a slow guided mode.

Besides, there is a noticeable oscillation in field magnitude at the opposite side of the source near the body [11,13]. This occurs due to the interference between the waves traveling clockwise and counter-clockwise. Since the waves propagate in two directions around the body, a two-wave model is set to fit the electric field distribution. Firstly, the wave propagating in a clockwise direction is identified as an exponentially decaying wave. To properly represent the transition region near the source, the exponent itself features an exponential transition from a value near the source to its value in the NLoS (Non-Line-of-Sight) region. The phase of such a wave simply varies at a linear rate, which means that a constant phase velocity is acceptable. A similar approximation is made for the wave propagating in an anti-clockwise direction. The equation for the fitted curve hence reads as:

$$E_{\mathrm{tot}} = 10^{(\alpha \exp(-\beta s)+\gamma+\delta s)/20}\, \mathrm{e}^{\mathrm{j}(\psi s+\phi)} + 10^{(\alpha \exp(-\beta (D-s))+\gamma+\delta (D-s))/20}\, \mathrm{e}^{\mathrm{j}(\psi (D-s)-\phi)} \tag{9}$$

Here, E_{tot} indicates the complex value of the normal component of electric field (radial electric field in V/m) and the field variation is investigated as a function of the distance around the curvature coordinate s. D is the perimeter of the cross-section. The coefficients α, β, γ, δ, ψ, ϕ are those required for the fitting of the wave model. The values of such coefficients for a circular cylinder and for an elliptical one are provided in Table 1 for normal polarization. Excellent fitting has been achieved, as can be seen in Fig. 5a. This means that a very simple propagation model can accurately represent the field along the body, including in the near-field region.

A simple fit has also been obtained for one of the elliptical cylinders, as in equation (9). The parameters for the clockwise wave are provided in the second line of Table 1. It is observed that the coefficients are quite similar for circular and elliptical cylinders. This essentially means that the propagation of surface waves for the case of normal polarization, in terms of both phase velocity and amplitude decay, have a very weak dependence on the cross-section of the cylinder for a certain perimeter; in other words, the creeping wave does not really "see" the shape of the scatterer. For the same reason, it is expected that the exact position of the source along the curved structure will have little impact. Further work may be devoted to estimating to which extent this is verified. However, a short study has been performed on these coefficients from

Table 1
Parameters for fitting the electric field distribution around circular and elliptical cylinders.

α dBV/m	β cm^{-1}	γ dBV/m	δ dBV/m cm^{-1}	ψ deg cm^{-1}	ϕ deg
14.55	0.42	−60.72	−0.943	−32.64	86.4
16.24	0.48	−63.25	−1.02	−34.43	85.0

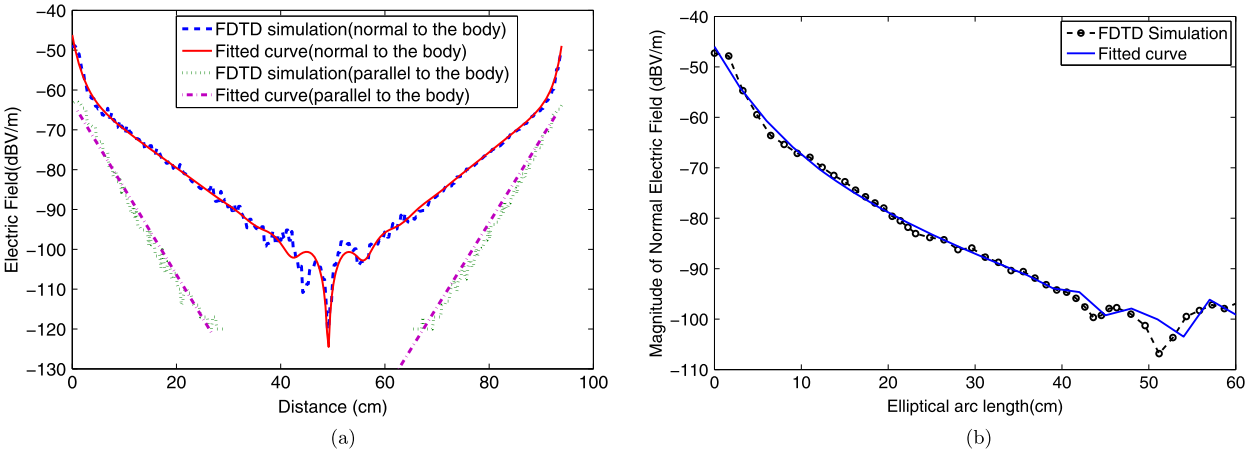

Fig. 5. (Color online.) Fitting between model and FDTD results, (a) for circular cylinder and vertical and normal polarizations, (b) for elliptical cylinder and normal polarization. Radius $a = 15$ cm.

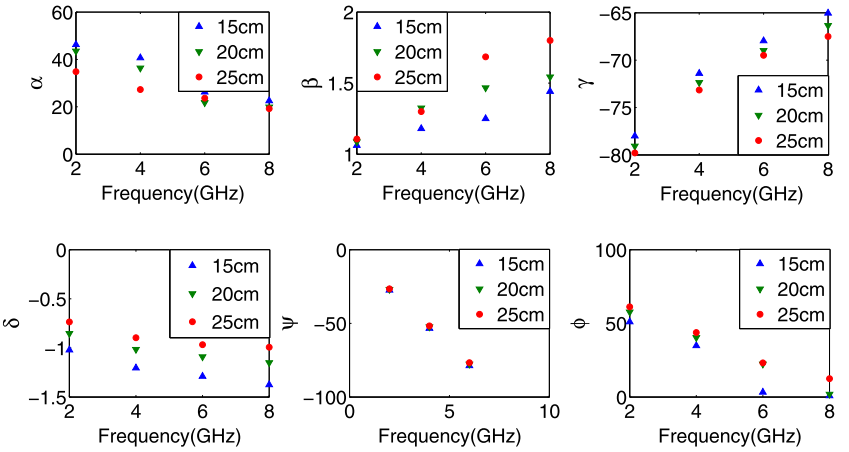

Fig. 6. (Color online.) Fitting coefficients versus frequency and versus radius. Radius $a = 15$ cm.

2–8 GHz for circular cylinders of 15, 20, and 25 cm. The results are provided in Fig. 6. It can be seen that all coefficients of the model have a relatively smooth behavior, which makes interpolation realistic, within the investigated range.

The phase velocities have been calculated from the normal components of electric fields for three elliptical cylinders, with axial ratios of $a/b = 1.14$, $a/b = 1.5$, and $a/b = 2$. The corresponding phase velocities obtained are $0.85\,c$, $0.87\,c$ and $0.88\,c$, respectively. Knowing that the phase velocity is $0.89\,c$ for $a/b = 1$, it is difficult to determine a trend for phase velocity versus axial ratio a/b; in other words it is remarkably independent of the exact shape of the cross section. A similar observation is made regarding the decay rate of the fields: as can be seen in Fig. 7a, between 10 and 20 cm, the rates of change in the electric field's components are very similar for the three elliptical cylinders. This is in line with the observation made in [28], where different cross sections are analyzed with the help of the Method of Moments. In other words, the phase velocity and the decay rate vary very little for change in shapes when the perimeter of the body is kept constant. In particular, for frequencies of a few GHz, the low phase velocity is typical for the creeping wave excited from normal-to-body sources, while a value very close to velocity of light, near $0.98c$, has been observed for fields radiated by sources tangential to the body. The latter value is very close to the one found in [52] for a similar configuration. Fig. 7b shows values of the phase velocity for increasing radii of the cylinder: it can be seen that phase velocity increases with radius, probably to approach the speed of light in free space when the surface becomes flat. It is interesting to note that, strictly speaking,

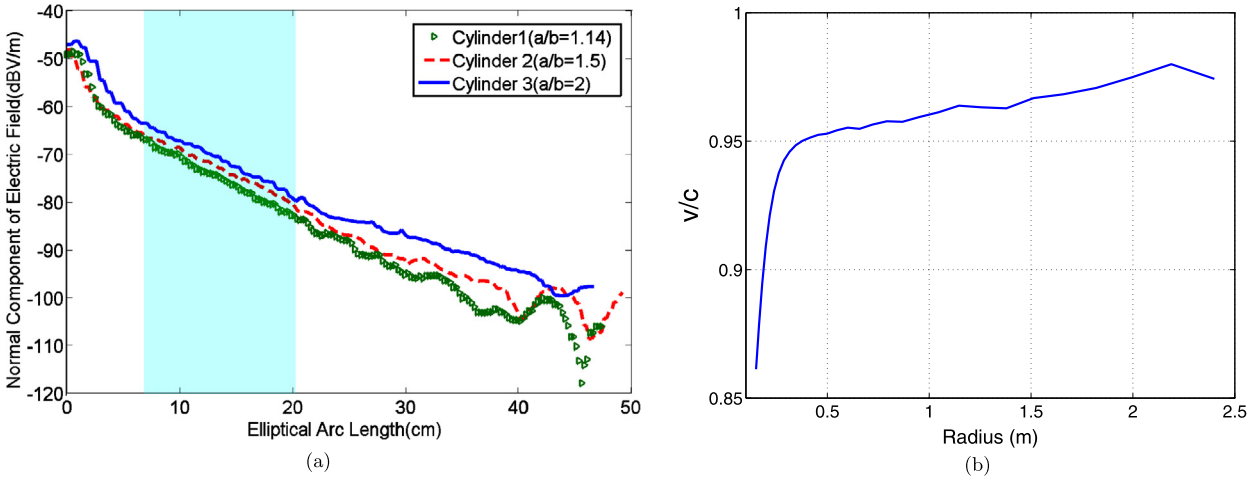

Fig. 7. (Color online.) (a) Decay of the normal electric field versus distance for elliptical cylinders with three different values of excentricity, (b) ratio between phase velocity and free-space velocity of light, versus cylinder radius for normal sources. Radius $a = 15$ cm.

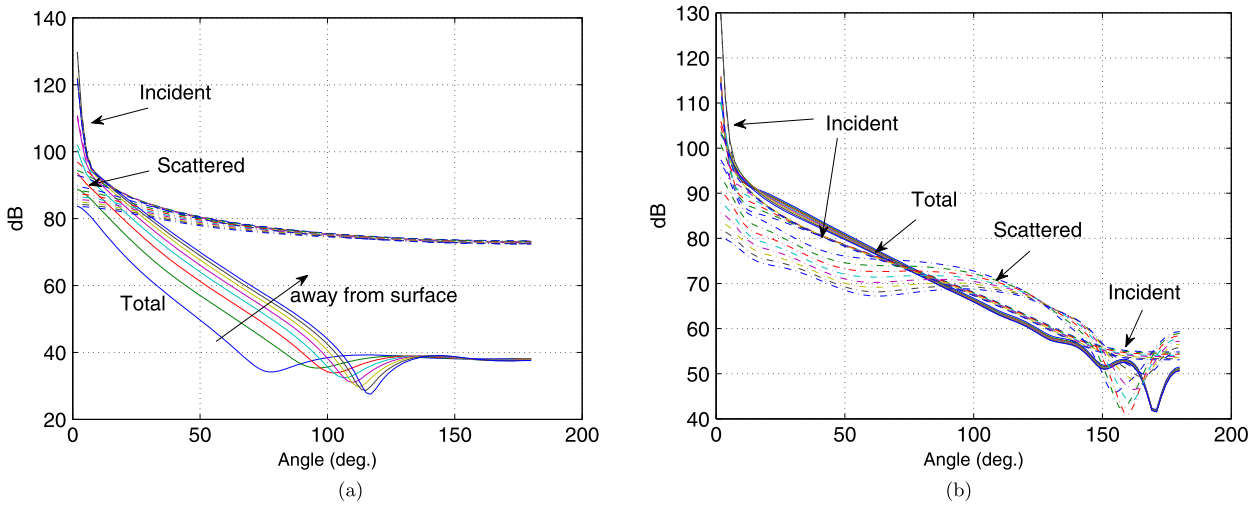

Fig. 8. (Color online.) Incident, scattered and total fields around the body, for different distance from body surface (0 to 3.5 cm, by steps of 0.5 cm): (a) vertical polarization, (b) normal polarization. Radius $a = 15$ cm.

the wave corresponding to the surface-wave pole, generally named the Zenneck wave ([29,30], Sec. 7.10), theoretically has a phase velocity larger than the speed of light. However, one should keep in mind that the Zenneck wave also decays exponentially in the direction of propagation and, as explained in [53] (Section 6.5), the corresponding pole contribution being only one among others, it gets canceled for very large distances and what remains is a more rapidly attenuating surface field, sometime called the Norton surface wave.[4] As a result, the phase velocity for the total fields may actually never exceed the speed of light in free space. The consistency of surface waves in the case of normal sources can be further analyzed through its decomposition into incident and scattered fields. That is done in Fig. 8 for a frequency of 2.45 GHz and a cylinder radius of 15 cm. Fig. 8a refers to vertical (i.e. parallel) sources and vertical fields. One can see how effectively the incident field gets short-circuited by the low-impedance surface: the incident and scattered fields have practically identical magnitudes and opposite phases, which leads to the very rapidly decaying total fields. As can be seen in Fig. 8b, this is not true in the case of the normal source. Very striking is the smooth but not linear (in log scale) behavior of the incident field and the quite complex shape of scattered fields, while the total fields produce a very straight dependence in log scale versus distance, which corresponds to a clear exponential decay of the total field, consistent with the proposed model (9)

[4] As Collin explained in [53], the Norton wave is not – strictly speaking – a surface wave, but it nonetheless corresponds to what is usually referred to as the surface-wave field. The Zenneck wave appears as an eigensolution for propagation with a complex wavenumber along the interface when one of the media is lossy; the Norton wave corresponds to the asymptotic behavior of the total fields when such an interface is illuminated by a normal current source.

away from the source. The dependence of the total field strength away from the interface, in the air, is quite weak, which is consistent with Zenneck waves.

4. Antenna analysis

Body Area Network antennas need to be placed very close to the body. Therefore, their radiation properties have essentially nothing in common with those they would have in free space, since the new radiating structure may now be considered as the superposition of the antenna and the body. As a result, unless specific designs are considered, both the impedance and the radiation pattern of the antenna are fundamentally impacted. Moreover, the quantity of interest does no longer correspond to far-field patterns, but it consists of the progression of the field along the surface of the body [54]. This leads to new rules for the design of body-area network antennas; those rules should for instance focus on the capability of the antenna to excite creeping waves along the body [1], and more generally on its ability to improve the link budget along the body [40], while preserving a low profile for the radiator. For instance, an antenna exploiting surface waves launched by a horizontally polarized antenna is proposed in [55]. The resilience of the antenna against direct effects of the body proximity have been mitigated through specific designs, through the use of screening backplanes [40], ferrite substrates [10] and inverted-F structures [56], naturally protruding from a ground plane [9], or through the use of short monopoles feed by a stripline [9,57].

In view of the complexity of the interaction between body and antenna and of the link between surface waves and their sources, numerical analysis is highly advisable. Here we consider the integral-equation approach, which presents the important advantage of limiting the unknown currents to the surface of the antenna itself. Indeed, the presence of the body and the radiation condition are implicitly included through the use of the Green functions described in Section 2. This will be explained below considering the canonic example of wire antennas. In a nutshell, using those Green's functions, the unknown currents are obtained by imposing the boundary conditions that the fields need to satisfy on the surface of the antennas. In turn, the method directly yields the transmittance between antennas accounting for both radiation and propagation effects. For instance, if the antenna is metallic, the additional condition to be satisfied is that the tangential electric field E_t be zero everywhere, except at the feed point, where it is imposed by the source voltage. For linear antennas, the integral equation reads:

$$E_{\mathrm{t}}(r) = \int_{l'} G^{\mathrm{inc}}(r, r')\, I(r')\, \mathrm{d}l' + \int_{l'} G^{\mathrm{scat}}(r, r')\, I(r')\, \mathrm{d}l' \tag{10}$$

where I is the current along the wire and G are the Green's functions tensors related to free space and to scattering by the cylinder, respectively. In their discretized form, the currents are decomposed into a set of pre-determined basis functions and the pertaining coefficients are obtained by solving a system of linear equations that enforce the boundary conditions on the antennas; this is the essence of the Method of Moments (MoM) [58].

To put this method into practice for antennas near cylinders, it is important to treat separately the incident and scattered fields. Here, by "incident field", we mean the field radiated when the antenna is in free space, while the "scattered field" only includes the effect of scattering by the cylinder. Then, the matrix that characterizes the system of equations can be regarded as the sum of two contributions, relating to the incident and scattered fields, associated with the two terms in (10). The incident fields actually should not be taken in harmonic form (1), because it does not converge when the observation point lies at the same radius as the source point. Instead, the matrix relating to the incident fields simply corresponds to the MoM matrix that one would have for the antenna in free space and as such fully includes the treatment of the singular aspect of the near fields [58], while the matrix relating to scattered fields is computed based only on the fields scattered by the body, which are in general regular. Mathematical expressions for those matrices can be found in [59] for antennas parallel to the body and in [24] for antennas normal to the body.

An example is given below for the impedance of an antenna parallel to the body, versus its distance from the body surface. The body radius is 15 cm, its relative permittivity is $47 - \mathrm{j}\,16$, the frequency is 2.45 GHz, the antenna length is near half-wavelength and its radius is 0.5 mm. Fig. 9a shows the reflection coefficient with respect to a reference impedance of 50 Ω[5] for two wire lengths, corresponding to wavelengths of 0.5 and 0.475, respectively. It can be seen that the matching of the antenna strongly fluctuates versus its distance from the body surface. The latter tends to "short-circuit" the antenna because of its low impedance, due primarily to its high real permittivity and, to a somewhat lower extent, to its conductivity.

The Green functions are exploited here to estimate the mutual coupling coefficients between antennas for vertical and normal polarizations. Contrary to the Green function taken alone, this mutual coupling result fully includes the effect of the antennas in the transmittance. This allows one to provide absolute levels without having to cater separately for the effect of antennas and of propagation losses. First, vertically oriented half-wave dipoles are placed at 1 cm from the body surface and they are azimuthally moved apart; the coupling coefficient is represented versus angular separation with a dashed curve in Fig. 9b. As can be expected from the Green function for this polarization, the coupling coefficient also rapidly falls off versus distance. It is not easy to say whether the flat region (dotted) is due to a creeping wave or to numerical roundoff;

[5] The reflection coefficient is calculated as $\Gamma = (Z - 50)/(Z + 50)$, where Z is the complex antenna impedance.

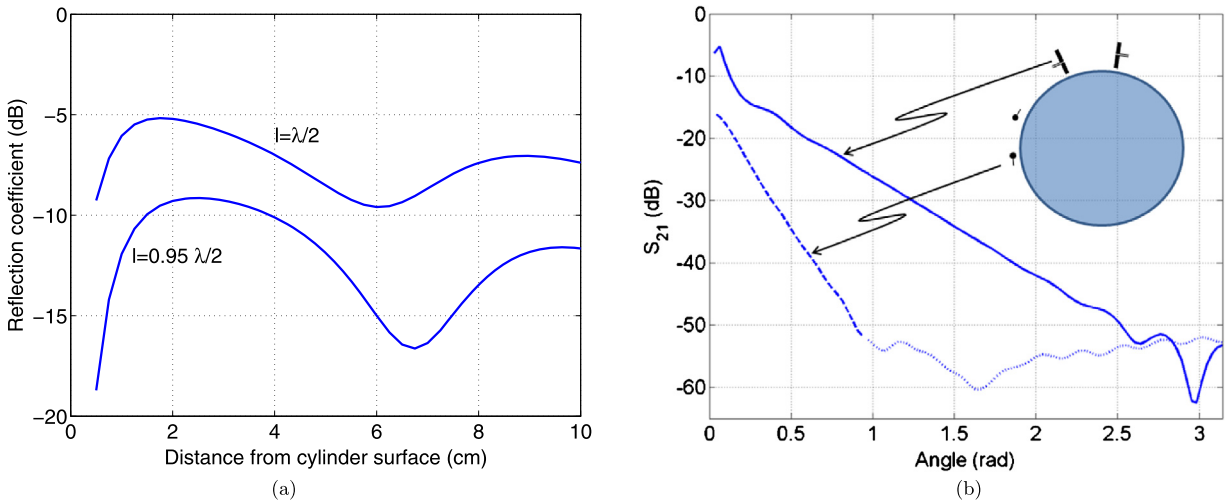

Fig. 9. (Color online.) (a) Matching of a vertically polarized antenna versus its distance from the cylinder's surface, (b) mutual coupling in dB in vertical–vertical (solid) and normal–normal configurations (dash–dot).

the latter is more plausible, which means that the coupling may be actually lower than calculated here. The coupling between normally-oriented antennas is shown considering radially-oriented half-wave antennas with one end located at 0.5 cm from the body surface. In this case, the coupling coefficient presents a slower and more steady decay versus the angular distance, a result that has been successfully validated in [24] through comparisons with data measured on an actual body. The very good comparison between measurements and simulations obtained in [24] for the normally-oriented case probably proceeds from the robustness mentioned in Section 3 of surface waves against the local curvature of the body. It is interesting to note that the integral-equation approach described here can be extended to the analysis of more complex and miniaturized antennas, possibly including dielectric material. That study can be implemented via the use of an equivalence surface [60,61], in order to distinguish the analysis of the inner part of the antenna from its interaction with the body. This should allow the analysis of more complex antennas, specifically devoted to the improvement of the budget link for body-to-body configurations.

5. Conclusions

Waves propagating along the body surface can be studied in first approximation while considering a cylindrical body, for which Green's functions can be computed analytically. In this operation, the conversion of point sources into a spectrum of line sources, and then into current sheets, plays a critical role. We extended this procedure to all source polarizations. We also proposed a matrix-form acceleration for the case where fields need to be observed over whole surfaces. The waves around the body analyzed in this way have been validated with the help of an FDTD software and a very simple and accurate model has been established. Waves radiated by sources perpendicular to the body surface are not strongly affected by the curvature of the body; their phase velocity is substantially low compared to the free-space wave velocity and it slowly increases as the radius of the body increases. Finally, we explained how the Green function can be exploited in an integral-equation scheme to determine the behavior of simple antennas in the presence of the body. In turn, this also allows the determination of coupling between two antennas located above the body surface while considering unknown currents on the antennas only. Such direct coupling analysis avoids the difficult issue of the contribution of the antennas themselves to the link budget along the body surface, for which radiation patterns cannot be used. Further research should focus on the analysis of more complex antennas that include a very short extension, though with substantial current level, normal to the body.

Appendix A. Field derivations

All field components can be derived from the components along z. This appendix recalls the corresponding relations, reproduced from [18]:

$$k_\rho^2 \vec{E}_s = -\mathrm{j}k_z \nabla_s E_z + \mathrm{j}k\eta\,\hat{z} \times \nabla_s H_z; \quad k_\rho^2 \vec{H}_s = -\mathrm{j}k_z \nabla_s H_z - \mathrm{j}k/\eta\,\hat{z} \times \nabla_s E_z \tag{11}$$

$$\text{with} \quad \nabla_s = \hat{\rho}\frac{\partial}{\partial\rho} + \hat{\phi}\frac{\mathrm{j}m}{\rho} \quad \text{and} \quad \hat{z} \times \nabla_s = \hat{\phi}\frac{\partial}{\partial\rho} - \hat{\rho}\frac{\mathrm{j}m}{\rho} \tag{12}$$

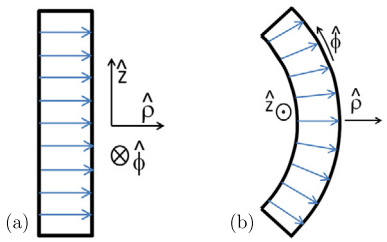

Fig. 10. (Color online.) Surface S of integration: (a) TM case, (b) TE case.

Appendix B. Boundary conditions

The boundary conditions across a sheet of normal currents are derived here. This derivation shares important steps with that providing the scalar Green's function [16]: integration of the wave equation over an infinitesimal domain, writing of the Laplacian as the derivative (or surface divergence $\nabla_s\cdot$) of another function and use of a relation of the Gauss' theorem family. The integrated wave equation for the magnetic field reads

$$\iint_S \nabla^2 \vec{H}\cdot\mathrm{d}\vec{S} + k^2 \iint_S \vec{H}\cdot\mathrm{d}\vec{S} = -\iint_S \nabla\times\vec{J}\cdot\mathrm{d}\vec{S} \tag{13}$$

where $\vec{J} = I\,\delta(\rho-\rho')\,\hat{\rho}/\rho'$. The infinitesimal surface S encloses a portion of the current sheet (Fig. 10).

In the *TM* case, since $H_z = 0$, the normal to the surface must be along $\hat{\phi}$ (Fig. 10a), hence requiring the ϕ component of the vector Laplacian in cylindrical coordinates [62]. Exploiting $\nabla\cdot\vec{H} = 0$, it can be obtained[6] as $(\nabla^2\vec{H})_\phi = \partial/\partial\rho\,\{(\nabla\times\vec{H})_z\} + \partial^2 H_\phi/\partial z^2$. Equation (13) then becomes

$$\iint \partial/\partial\rho\,\{(\nabla\times\vec{H})_z\}\,\mathrm{d}S + \iint \partial^2 H_\phi/\partial z^2\,\mathrm{d}S + k^2 \iint \vec{H}\cdot\mathrm{d}\vec{S} = -\iint \nabla\times\vec{J}\cdot\mathrm{d}\vec{S} \tag{14}$$

$$\int [(\nabla\times\vec{H})_z]_{\rho^-}^{\rho^+}\,\mathrm{d}z + (k^2 - k_z^2)\iint \vec{H}\cdot\mathrm{d}\vec{S} = -\oint \vec{J}\cdot\mathrm{d}\vec{l} \tag{15}$$

$$\mathrm{j}\frac{k}{\eta}\,\Delta E_z\,\mathrm{d}z + k_\rho^2\cdot 0 = -(I(z+\mathrm{d}z) - I(z))/\rho' \tag{16}$$

where $\Delta P = P(\rho^+) - P(\rho^-)$. The final right-hand side results from integrating twice the Dirac delta function of the current sheet along the contour. Result (16) provides the first condition in (3).

In the *TE* case, since $H_z \neq 0$, the normal to the surface is taken along $\hat{z}$ (Fig. 10b). Following essentially the same procedure as for the TM case, we have:

$$\iint (\nabla_s\cdot\nabla H_z + \partial^2 H_z/\partial z^2)\,\mathrm{d}S + k^2 \iint \vec{H}\cdot\mathrm{d}\vec{S} = -\iint \nabla\times\vec{J}\cdot\mathrm{d}\vec{S} \tag{17}$$

$$\oint \nabla H_z\,.\,\hat{n}_l\,\mathrm{d}l + (k^2 - k_z^2)\iint \vec{H}\cdot\mathrm{d}\vec{S} = -\oint \vec{J}\cdot\mathrm{d}\vec{l} \tag{18}$$

$$\Delta\,\{\partial H_z/\partial\rho\}\;\rho'\,\mathrm{d}\phi + k_\rho^2\cdot 0 = (I(\phi+\mathrm{d}\phi) - I(\phi))\,/\rho' \tag{19}$$

where $\hat{n}_l$ is the unit vector normal to the edge. This provides the second condition in (3).

The corresponding result for flat surfaces can be written as $\Delta\vec{E} = \mathrm{j}\,\eta/k\,\nabla J$. It can be verified that the TM condition (16) coincides with that result and that the TE condition (19) coincides for ρ' tending toward infinity. It has also been verified that, following the procedure described in Section 2, conditions (3) produce exactly the same expressions for TE and TM fields as when the addition theorem is used.[7]

References

[1] A. Lea, P. Hui, J. Ollikainen, R.G. Vaughan, Propagation between on-body antennas, IEEE Trans. Antennas Propag. 57 (2009) 3619–3627.
[2] G.A. Conway, et al., An analytical path-loss model for on-body radio propagation, in: URSI International Symposium, 2010, pp. 332–335.
[3] L. Petrillo, et al., Analytical creeping wave model and measurements for 60 GHz body area networks, IEEE Trans. Antennas Propag. 62 (2014) 4352–4356.

[6] In short, expressing differential operators in cylindrical coordinates [62] and denoting $\partial P/\partial v$ as P^v, $\nabla\cdot\vec{H} = 0$ produces $H_\rho^{\rho\phi} = -(H_\rho^\phi + H_\phi^{\phi\phi})/\rho$, which appears in $(\nabla\times H)_z^\rho$. A replacement produces $(\nabla^2 H)_\phi$, without the H_ϕ^{zz} term.

[7] This can be verified by noting that in [24], a $1/4\,\mathrm{j}$ factor is missing in (8) and (9) and that, in (10), $Q_m = -k_\rho\,J_m(k_\rho\,\rho)$, by virtue of the equation that defines Bessel's functions.

[4] J. Ryckaert, P. De Doncker, Channel model for wireless communication around human body, Electron. Lett. 40 (2004) 543–544.
[5] S.L. Cotton, R. D'Errico, C. Oestges, A review of radio channel models for body centric communications, Radio Sci. 49 (2014) 371–388.
[6] W. Scanlon, N. Evans, Numerical analysis of bodyworn UHF antenna systems, Electron. Commun. Eng. J. 13 (2001) 53–64.
[7] P.S. Hall, Y. Hao, Antennas and Propagation for Body-Centric Wireless Communications, Artech House, Norwood, MA, USA, 2006.
[8] P. Hall, et al., Antennas and propagation for on-body communication systems, IEEE Trans. Antennas Propag. 49 (2007) 41–58.
[9] C. Roblin, et al., Antenna design and channel modeling in the BAN context – part I: antennas, Ann. Telecommun. (2011) 139–155.
[10] T. Alves, et al., Polymeric ferrite-loaded antennas for on-body communications, Microw. Opt. Technol. Lett. 11 (2009) 2530–2533.
[11] A. Fort, et al., A body area propagation model derived from fundamental principles: analytical analysis and comparison with measurements, IEEE Trans. Antennas Propag. 58 (2010) 503–514.
[12] A.M. Eid, N. Murtaza, J.W. Wallace, Green's function models and measurements for body area network (BAN) channels, in: IEEE Int. Conf. Wireless Inf. Tech. Sys., 2010.
[13] T. Alves, B. Poussot, J.M. Laheurte, Analytical propagation modeling of BAN channels based on the creeping-wave theory, IEEE Trans. Antennas Propag. 59 (2011) 1269–1274.
[14] L. Liu, et al., An analytical modeling of polarized time-variant on-body propagation channels with dynamic body scattering, EURASIP J. Wirel. Commun. Netw. (2011) 1–15.
[15] Iswandi, et al., The utilization of body skeleton model for modeling the dynamic BAN channels, in: Proc. European Conference on Antennas and Propagation, EuCAP, 2012, pp. 540–543.
[16] C.-T. Tai, Dyadic Green's Functions in Electromagnetic Theory, 2nd ed., IEEE Press, New York, 1994.
[17] A. Taflove, Computational Electrodynamics: The Finite-Difference Time-Domain Method, 2nd ed., Artech House, Norwood, MA, 2000.
[18] W.C. Chew, Waves and Fields in Inhomogeneous Media, IEEE Press, New York, 1995.
[19] K. Michalski, J. Mosig, Multilayered media Green's functions in integral equation formulations, IEEE Trans. Antennas Propag. 45 (1997) 508–519.
[20] P.M. Morse, H. Feshbach, Methods of Theoretical Physics, McGraw-Hill, New York, 1953.
[21] J.S. Bever, J.P. Allebach, Multiple scattering by a planar array of parallel dielectric cylinders, Appl. Opt. 31 (1992) 3524–3531.
[22] G. Roqueta, A. Fort, C. Craeye, C. Oestges, Analytical propagation models for body area networks, in: Proc. IET Seminar on Antennas and Propagation for Body-Centric Wireless Communications, 24 April 2007, pp. 90–96.
[23] F. Keshmiri, C. Craeye, Wave propagation from sources with arbitrary polarization next to the human body, in: Proc. IEEE APS/USNC/URSI International Symposium, Toronto, 2010.
[24] F. Keshmiri, C. Craeye, Moment-method analysis of normal-to-body antennas using a Green's function approach, IEEE Trans. Antennas Propag. 60 (2012) 4259–4270.
[25] L. Beyne, D. De Zutter, Green's function for layered media with special application to microstrip antennas, IEEE Trans. Microw. Theory Tech. 36 (1988) 875–881.
[26] A. Khaleghi, I. Balasigham, Non-line-of-sight on-body ultra wideband (1–6 GHz) channel characterisation using different antenna polarisations, IET Microw. Antennas Propag. 3 (2009) 1019–1027.
[27] L. Akhoondzadeh-Asl, I. Khan, P.S. Hall, Polarisation diversity performance for on-body communication applications, IET Microw. Antennas Propag. 5 (2011) 232–236.
[28] A.M. Eid, J.W. Wallace, Accurate modeling of body area network channels using surface-based method of moments, IEEE Trans. Antennas Propag. 59 (2011) 3022–3030.
[29] J. Wait, The ancient and modern history of EM ground-wave propagation, IEEE Antennas Propag. Mag. 40 (5) (1998) 7–24.
[30] S. Orfanidis, Electromagnetic Waves and Antennas, Rutgers Univ. Ed., 2008.
[31] K.A. Norton, The propagation of radio waves over the surface of the earth and in the upper atmosphere, Proc. Inst. Radio Eng. 24 (1937) 1203–1236.
[32] N. Chahat, G. Valerio, M. Zhadobov, R. Sauleau, On-body propagation at 60 GHz, IEEE Trans. Antennas Propag. 61 (2013) 1876–1888.
[33] N. Chahat, M. Zhadobov, R. Sauleau, K. Ito, A compact UWB antenna for on-body applications, IEEE Trans. Antennas Propag. 59 (2011) 1123–1131.
[34] R. Paknys, N. Wang, High-frequency surface field excited by a magnetic line source on an impedance cylinder, IEEE Trans. Antennas Propag. 35 (1987) 293–298.
[35] G.N. Watson, The diffraction of electric waves by the Earth, Proc. R. Soc. Lond. A 95 (1918) 83–99.
[36] C.A. Balanis, Antenna Theory: Analysis and Design, 3rd ed., Wiley, New York, 2005.
[37] D. Ma, W.X. Zhang, Analytic propagation model for wireless body-area networks, IEEE Trans. Antennas Propag. 59 (2011) 4749–4756.
[38] S. Dumanli, C.J. Railton, Analysis of coupled tilted slot antennas in FDTD using a novel time domain Huygens method with application to body area networks, IEEE Trans. Antennas Propag. 60 (2012) 1987–1994.
[39] W.-T. Shay, S.-C. Jan, J.-H. Tarng, A reduced-size wide slot antenna for enhancing along-body radio propagation in UWB on-body communications, IEEE Trans. Antennas Propag. 62 (2014) 1194–1203.
[40] Y.-F. Wei, C. Roblin, Multi-slot antenna with a screening backplane for UWB BAN applications, Int. J. Antennas Propag. 2012 (2012) 731912.
[41] J.-P. Berenger, A perfectly matched layer for the absorption of electromagnetic waves, J. Comput. Phys. 114 (1994) 185–200.
[42] J.Y. Chen, O.P. Gandhi, Currents induced in an anatomically based model of a human for exposure to vertically polarized electromagnetic pulses, IEEE Trans. Microw. Theory Tech. 39 (1991) 31–39.
[43] V. Spitzer, et al., The visible human male: a technical report, J. Am. Med. Inform. Assoc. 3 (1996) 118–130.
[44] P.J. Dimbylow, FDTD calculations of the whole-body averaged SAR in an anatomically realistic voxel model of the human body from 1 MHz to 1 GHz, Phys. Med. Biol. 42 (1997) 479–490.
[45] S.-L. Lee, K. Ali, et al., A whole body statistical shape model for radio frequency simulation, in: Proc. 2011 Annual International Conference of the IEEE, Engineering in Medicine and Biology Society, EMBC, 2011, pp. 7143–7146.
[46] A. Sani, et al., An efficient FDTD algorithm based on the equivalence principle for analyzing on-body antenna performance, IEEE Trans. Antennas Propag. 57 (2009) 1006–1014.
[47] K. Ali, et al., Quantitative estimation of subject specific on-body propagation channel, Antennas Wirel. Propag. Lett. 14 (2014) 398–401.
[48] Q.H. Abbasi, et al., Numerical characterization and modelling of subject-specific ultra wide band body-centric radio channels and systems for healthcare applications, IEEE Trans. Inf. Technol. Biomed. 16 (2012) 221–227.
[49] Italian National Research Council – Institute for Applied Physics, Dielectric properties of body tissues in the frequency range 10 Hz–100 GHz, INRC, 2012 [online]. Available: http://niremf.ifac.cnr.it/tissprop/.
[50] P. Min, http://www.cs.princeton.edu/~min/binvox/.
[51] IEEE Standard definitions of terms for radio wave propagation, 1997.
[52] S. van Roy, et al., On-body propagation velocity estimation using ultra-wideband frequency-domain spatial correlation analyses, Electron. Lett. 43 (2007) 1405–1406.
[53] R. Collin, Antennas and Radiowave Propagation, McGraw-Hill, New York, 1985.
[54] Z. Ma, et al., Antenna radiation characteristics for on-body communication channel using creeping-wave theory, in: Proc. European Conference on Antennas and Propagation, EuCAP, 2015.

[55] L. Akhoondzadeh-Asl, Y. Nechayev, P.S. Hall, C. Constantinou, Parasitic array antenna with enhanced surface wave launching for on-body communications, IEEE Trans. Antennas Propag. 61 (2013) 1976–1985.
[56] C.H. Lin, K. Saito, M. Takahashi, K. Ito, A compact planar inverted-F antenna for 2.45 GHz on-body communication, IEEE Trans. Antennas Propag. 60 (2012) 4422–4426.
[57] F. Keshmiri, Body-Area-Network antennas: Green's functions, numerical analysis and design, Ph.D. thesis, Université catholique de Louvain, Belgium, February 2012.
[58] R.F. Harrington, Field Computation by Moment Methods, Wiley–IEEE Press, New York, 1993.
[59] F. Keshmiri, C. Craeye, A Green's function approach for analysis of body-area-network antennas, in: LAPC Antennas and Propagat. Conf., Loughborough, UK, 2009.
[60] R.F. Harrington, Time-Harmonic Electromagnetic Fields, McGraw-Hill, New York, 1961.
[61] S.M. Rao, D.R. Wilton, E-field, H-field, and combined field solution for arbitrarily shaped three-dimensional dielectric bodies, Electromagnetics 10 (1990) 407–421.
[62] B. Maxum, Field Mathematics for Electromagnetics, Photonics and Materials Science, SPIE Library, Washington D.C., 2007.